

Solar primary and secondary ionization at Saturn

Marina Galand,¹ Luke Moore,² Benjamin Charnay,³ Ingo Mueller-Wodarg,¹ and Michael Mendillo²

Received 9 December 2008; revised 5 March 2009; accepted 6 April 2009; published 19 June 2009.

[1] Solar EUV and soft X-ray photons are a prime source of energy upon Saturn's upper atmosphere. In particular, they represent a significant source of ionization yielding the creation of an ionosphere, a region probed by the Cassini Radio Science Subsystem (RSS) experiment. During the past decade the only ionization process modeled at Saturn under solar illumination has been photoionization. We present the first detailed calculation of the ionization rate by suprathermal electrons (photoelectrons and their secondaries), applied to Saturn using realistic solar flux and neutral atmospheric input. The energy degradation model, describing the absorption of solar photons and the transport of suprathermal electrons, is self-consistently coupled with an ionospheric model providing the electron and ion densities and temperatures. The coupled model is applied to equinox conditions at 30°N latitude. We assess and compare the photoionization and electron-impact ionization rates. We discuss their sensitivity with solar flux models as well as solar activity. We find that the secondary production rate affects not only the bottom side of the ionosphere, as previously predicted, but also the main ionospheric peak. The electron density is increased by up to 30% at the peak with a decrease in the peak altitude by several hundreds of kilometers around local noon. Above the homopause, the largest increase in electron density is found after sunrise below the ionospheric peak. Finally, we compare the energy degradation of photoelectrons with auroral electrons and discuss the relevance of this study to the interpretation of observations by the Cassini RSS and Cassini Plasma Science/Electron Spectrometer instruments.

Citation: Galand, M., L. Moore, B. Charnay, I. Mueller-Wodarg, and M. Mendillo (2009), Solar primary and secondary ionization at Saturn, *J. Geophys. Res.*, 114, A06313, doi:10.1029/2008JA013981.

1. Introduction

[2] The six dawn and dusk radio occultations from Pioneer 11 and Voyager 1 and 2 were acquired during solar maximum conditions (1979–1981) and covered a wide range of latitudes. They have revealed a highly variable and complex structure for Saturn's ionosphere [Kliore *et al.*, 1980a, 1980b; Tyler *et al.*, 1981, 1982; Atreya *et al.*, 1984; Lindal *et al.*, 1985]. The derived profiles show a peak in electron density of $0.6\text{--}2 \times 10^4 \text{ cm}^{-3}$, with a peak altitude ranging from 1800 to 2900 km above the 1 bar level, and multiple secondary peaks at lower altitudes with magnitudes occasionally very close to the main peaks. More recently, the Radio Science Subsystem (RSS) onboard the Cassini orbiter has provided a new set of electron density profiles during low solar activity. The first published set includes twelve dawn and dusk profiles obtained from near-equatorial occultations [Nagy *et al.*, 2006]. They show an upper altitude peak with a density between $\sim 5 \times 10^2 \text{ cm}^{-3}$

and $7 \times 10^3 \text{ cm}^{-3}$ at an altitude ranging from 1850 km to 3000 km, a lower-altitude peak with a density between $4 \times 10^2 \text{ cm}^{-3}$ and $8 \times 10^3 \text{ cm}^{-3}$ at an altitude ranging from 1150 to 1800 km and additional tertiary peaks at lower altitudes. The second published set includes nineteen new occultations, seven from midlatitudes ($20^\circ < |\text{lat}| < 60^\circ$) and eight from high latitudes ($|\text{lat}| > 60^\circ$), and reaffirms the highly structured and variable ionosphere of Saturn [Kliore *et al.*, 2009]. Averaging the profiles over latitude regions reveals an increase of the electron density with latitude, which may be due to additional particle ionization sources or a reduction of loss sources with latitude [Kliore *et al.*, 2009].

[3] The main source of dayside ionization yielding the creation of an ionosphere is solar irradiance from soft X rays (0.1–10 nm) to the extreme ultraviolet (EUV) (10–110 nm) and far ultraviolet (FUV) (110–200 nm) [e.g., Moses and Bass, 2000]. Before the first radio occultation was made available, models of Saturn's ionosphere overpredicted the electron density peak by one order of magnitude and underpredicted its altitude [e.g., McElroy, 1973; Atreya and Donahue, 1975; Capone *et al.*, 1977]. In an attempt to reconcile modeled results with radio occultation observations, two loss processes of H^+ , a long-lived and dominant ion in Saturn's ionosphere, have been invoked. One is the charge-exchange reaction between vibrationally excited H_2 ($\nu \geq 4$) with H^+ and the other is the influx of

¹Department of Physics, Imperial College London, London, UK.

²Center for Space Physics, Boston University, Boston, Massachusetts, USA.

³Ecole Normale Supérieure de Lyon, Lyon, France.

water or of OH from Saturn's rings, yielding the depletion of H^+ and the production of short-lived molecular ions [e.g., *McElroy*, 1973; *Connerney and Waite*, 1984; *Majeed and McConnell*, 1991]. Results from a comprehensive model including 1-D water diffusion calculations showed that a constant influx of water of $(0.5-1.0) \times 10^7 \text{ cm}^{-2} \cdot \text{s}^{-1}$ is adequate for reproducing the near-equatorial Cassini measurements [*Moore et al.*, 2006], which might reduce the necessity of charge exchange of H^+ with vibrationally excited H_2 , in agreement with recent theoretical work [*Huestis*, 2008]. Other candidates for reducing the electron density at the peak include vertical transport of plasma by either neutral winds or electric fields, or diurnal changes in electron density profiles associated with upward/downward plasmaspheric fluxes [e.g., *Majeed and McConnell*, 1991]. These quantities are, however, very poorly constrained. Another process affecting the electron density structures is the shadowing by Saturn's rings [*Moore et al.*, 2004; *Mendillo et al.*, 2005]. Finally, metallic ions of meteoritic origin, cosmic ray ionization, and atmospheric gravity waves [e.g., *Capone et al.*, 1977; *Moses and Bass*, 2000] could account for sporadic layers in the deep ionosphere.

[4] Under solar illumination, atmospheric neutral species are ionized by solar photons. While usually included in the case of Venus, Earth, Mars, Jupiter, and Titan [e.g., *Kim and Fox*, 1994; *Schlesier and Buonsanto*, 1999; *Cravens et al.*, 2004; *Fox and Yeager*, 2006; *Galand et al.*, 2006; *Fox*, 2007], the contribution by photoelectrons as an additional source of energy is often neglected in ionospheric models applied to Saturn [e.g., *Moses and Bass*, 2000; *Moore et al.*, 2004, 2006]. In support of the interpretation of the radio occultation observations, it is important to assess how and by how much this additional ionization source affects the electron density profile. Photoelectrons produced by energetic solar photons have enough energy to interact subsequently with the atmosphere. Such an interaction yields heating of the ionospheric thermal electrons and additional ionization of the neutral atmospheric species. On the basis of extrapolation from Jovian calculations by *Kim and Fox* [1994], *Moses and Bass* [2000] predicted that neglecting the electron-impact ionization by photoelectrons and their secondaries would yield an underestimation of the H_2^+ production rate (and consequently of the electron production rate) at Saturn, especially in the bottomside of the ionosphere. The only ionospheric modeling study taking into account the contribution of photoelectrons and their secondaries in Saturn's ionosphere was presented by *Waite* [1981]. However, because of poor constraints on the neutral atmosphere at that time, the thermospheric model used by *Waite* [1981] is not realistic with an exospheric temperature near 1000 K, significantly larger than the now accepted value of 420 K [*Smith et al.*, 1983; *Hubbard et al.*, 1997]. As a result, *Waite* [1981] overestimated neutral densities above the homopause with values several orders of magnitude larger than what the current estimate provides. Another strong limitation of that study is the solar flux model based on *Torr et al.* [1979]. While at the time, this empirical model provided the best available estimate of solar flux, it is poorly constrained over the soft X-ray region, with only one bin (5–10 nm) over this spectral region. Starting at 5 nm, it neglects the part of the solar spectrum most efficient in

producing energetic photoelectrons, and thus greatly underestimates the production rate due to electron impact.

[5] In the following we attempt to quantify the contribution of photoelectrons (and their secondaries) to Saturn's ionosphere using the latest constraints on neutral atmospheric and solar conditions as well as newly developed models. Parameterizations of the thermal electron heating and electron-impact ionization rates by photoelectrons have been developed by *Moore et al.* [2008] and *Moore et al.* [2009], two companion papers to the present study. The effectiveness of these two parameterizations over a range of seasons and latitudes is discussed by *Moore et al.* [2009]. The contribution of photoelectrons to the ionospheric temperatures has been discussed in detail by *Moore et al.* [2008] and will not be repeated here. In the present paper, we focus on the effect of photoelectrons as a source of ionization for Saturn's upper atmosphere.

2. Model

2.1. Coupled Model

[6] In order to assess the contribution of photoelectrons and associated secondary electrons to the ionospheric state, we have coupled two comprehensive models, as part of the Saturn Thermosphere-Ionosphere Model (STIM) effort, a suite of 1-D, 2-D, and 3-D models developed to study Saturn's upper atmosphere [e.g., *Moore et al.*, 2004; *Mueller-Wodarg et al.*, 2006]. The energy deposition model describes the attenuation of the solar photon flux through absorption by atmospheric neutrals and the transport and energy degradation of the induced suprathermal electrons. The ionospheric model calculates the densities, drift velocities, and temperatures of the thermal ionospheric population by solving the continuity, momentum, and energy equations for the ionospheric species. Both models are coupled in a self-consistent manner. On one hand, the altitude profiles of the thermal electron density and temperature computed by the ionospheric model are used as an input to the suprathermal electron transport model to assess the energy transfer through Coulomb collisions between the suprathermal and the thermal electrons. On the other hand, the energy deposition model provides the ionospheric model with the altitude profiles of the ion production rates, source terms of the ion continuity equations, and the thermal electron heating rates that are a source term of the electron energy equation. Physical quantities are exchanged at a 10 Saturn minute time resolution (~ 4.44 minutes) in order to resolve the quickly changing dawn and dusk ionosphere. The coupling process between both models is repeated until convergence is reached, which typically occurs after two iterations. A more detailed description of the coupled model is given in the companion paper by *Moore et al.* [2008].

[7] The energy degradation and the ionospheric models are both driven by the same atmospheric and solar conditions. The neutral densities (see Figure 1) are taken from a 1-D version of the gas diffusion model used in the STIM General Circulation Model (GCM) of *Mueller-Wodarg et al.* [2006], assuming an eddy coefficient as inferred by *Moses et al.* [2000a]. Neutral temperatures are consistent with observations as summarized by *Moses et al.* [2000a], which are valid for midlatitude regions. The modeled altitude range is from 600 to 3000 km above the 1-bar level. One

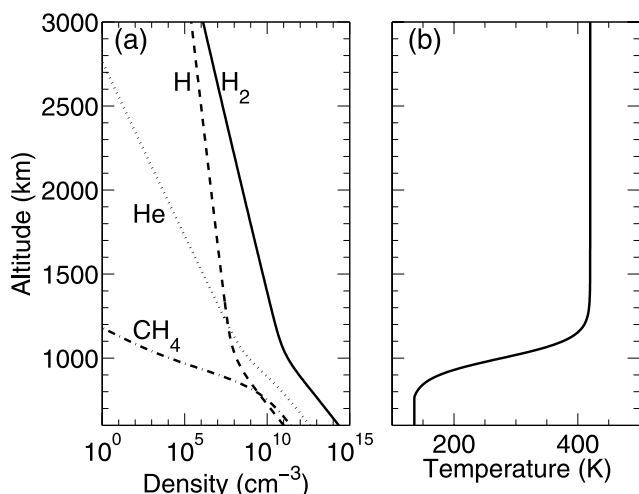


Figure 1. Neutral atmospheric (a) density and (b) temperature profiles in altitude resulting from the 1-D neutral STIM (see section 2.1).

noteworthy feature clearly apparent in the density profiles of the three main neutral species (H₂, H, He) is the sharp change in gradient around 1000 km corresponding to the transition from a “mixing” region to a region where gases are diffusively separated. As the helium and hydrogen species are significantly lighter than the hydrocarbons, the diffusive separation yields a large increase in the scale height of the light species, resulting in this sharp change in gradient. Because of sparse published data set of photoionization cross sections for hydrocarbons (e.g., CH₃), we treat the hydrocarbon layer here as consisting purely of methane, i.e., it is used as a marker for this layer. For relevance to the Cassini mission, we have chosen ~2008–2009 conditions, that is, equinox with a 0° solar declination and solar cycle minimum conditions. Solar irradiance is the only incident energy source considered. This study focuses on midlatitude (30°N) where solar photons are most likely the dominant source of ionization. The default solar flux assumed is described in section 2.2. The magnetic field configuration is based on the Saturn Pioneer Voyager model [Davis and Smith, 1990].

2.2. Energy Deposition Model

[8] The energy deposition model solves the Beer-Lambert law describing the absorption of solar photons in the upper atmosphere. An explicit integration along the line of sight is included (as opposed to using a Chapman approximation), allowing accurate calculation of the absorbed solar flux also for solar zenith angles (sza) above 75°. From the absorbed solar flux, the photoelectron production rate, hereafter called primary production rate, is derived. The transport and energy degradation of the photoelectrons and associated secondary electrons in the upper atmosphere are assessed by solving the Boltzmann equation for suprathermal electrons. The multistream transport model is based on the solution proposed by Lummerzheim *et al.* [1989] for terrestrial applications and has been validated through comparison with laboratory measurements [Lummerzheim and Liliensten, 1994]. It has previously been adapted to Titan’s ionosphere

[Galand *et al.*, 1999, 2006] and recently to Saturn’s ionosphere [Moore *et al.*, 2008]. The energy range considered for the suprathermal electrons is 0.1 eV to 10 keV over 300 levels. An 8-level Gaussian pitch angle grid is used.

[9] The photoabsorption and photoionization cross section set has been updated from the original data set proposed by Moore *et al.* [2004]. First, the wavelength resolution has been increased from the old standard of 39 bins to a 1-nm grid on which the solar flux is now commonly given. Another noteworthy difference between the two sets is the dissociative ionization cross sections of H₂, with an increase in the photoionization of H₂ yielding H⁺ + H below 40 nm. Updated photoabsorption and photoionization cross sections are presented in Figure 2.

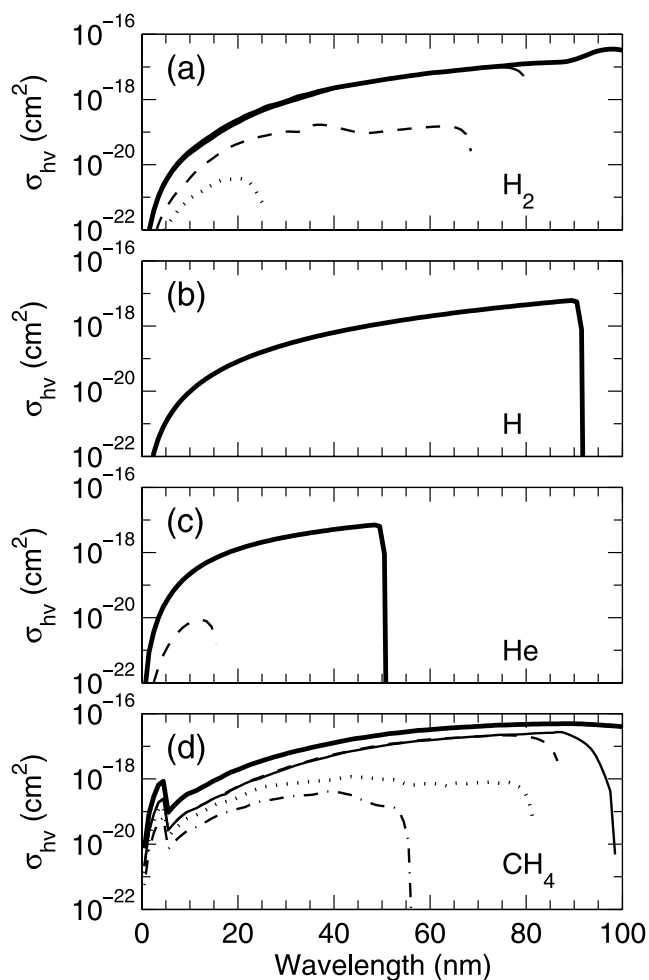


Figure 2. Photoabsorption (thick lines) and photoionization (thin lines) cross sections for the neutral species considered: (a) H₂, (b) H, (c) He, and (d) CH₄. For H₂, the ionization cross sections shown correspond to the production of H₂⁺ (thin, solid line), H⁺ + H (dashed line), and 2H⁺ (dotted line). For He, the ionization cross sections shown correspond to the production of He⁺ (thin, solid line), undistinguishable in Figure 2 from the photoabsorption cross section (thick, solid line) and He²⁺ (dashed line). For CH₄, only the ionization cross sections for the four main ions are shown, that is, CH₄⁺ (thin, solid line), CH₃⁺ (dashed line), CH₂⁺ (dotted line), and CH⁺ (dash-dotted line).

Table 1. Reference List for the Photoimpact and Electron-Impact Cross Sections

| Reaction | References Used for Compilation |
|--------------------------------|---|
| $H + hv \rightarrow H^+$ | <i>Verner et al.</i> [1996] |
| $He + hv \rightarrow He^+$ | <i>Verner et al.</i> [1996] |
| $H_2 + hv$ | <i>Backx et al.</i> [1976], <i>Yan et al.</i> [1998] |
| $H_2 + hv \rightarrow H_2^+$ | <i>Backx et al.</i> [1976], <i>Kossmann et al.</i> [1989a], <i>Chung et al.</i> [1993], <i>Yan et al.</i> [1998] |
| $H_2 + hv \rightarrow H^+ + H$ | <i>Chung et al.</i> [1993] and $2H^+$ references |
| $H_2 + hv \rightarrow 2H^+$ | <i>Dujardin et al.</i> [1987], <i>Kossmann et al.</i> [1989b] <i>Yan et al.</i> [1998] |
| $CH_4 + hv$ | <i>Samson et al.</i> [1989], <i>Schunk and Nagy</i> [2000] same references for ionization producing CH_4^+ , CH_3^+ , CH_2^+ , CH^+ , C^+ |
| $H + e^-$ | <i>Brackmann et al.</i> [1958], <i>Burke and Smith</i> [1962], <i>Bray et al.</i> [1991], <i>Mayol and Salvat</i> [1997], <i>Stone et al.</i> [2002], <i>Bartlett and Stelbovics</i> [2004] |
| $He + e^-$ | <i>LaBahn and Callaway</i> [1970], <i>Mayol and Salvat</i> [1997], <i>Stone et al.</i> [2002], <i>Bartlett and Stelbovics</i> [2004] |
| $H_2 + e^-$ | <i>van Wingerden et al.</i> [1980], <i>Ajello et al.</i> [1991], <i>Jain and Baluja</i> [1992], <i>Straub et al.</i> [1996], <i>Liu et al.</i> [1998], <i>Brunger and Buckman</i> [2002] |
| $CH_4 + e^-$ | <i>Davies et al.</i> [1989], <i>Liu and Shemansky</i> [2006] |

The complete list of references used for compiling the photoimpact and electron-impact cross sections is given in Table 1.

[10] The default solar flux at the top of the atmosphere is based on the measurements of the Thermosphere Ionosphere Mesosphere Energetics and Dynamics (TIMED)/Solar EUV Experiment (SEE) extrapolated to Saturn under solar minimum conditions [*Woods et al.*, 2000, 2005; *Woods*, 2008]. The extrapolation takes into account both the distance correction and the phasing over time (or time shift). The latter corresponds to the difference in solar longitude between Earth and Saturn. It is critical to take it into account for solar maximum conditions which are discussed in Appendices A and B. The daily average level 3 data product (version 9) was used, which provides the solar flux on a 1-nm interval over the 0.5 to 194.5 nm range (<http://lasp.colorado.edu/see/>). The default day chosen is 15 May 2008, associated with a daily solar index $F_{10.7}$ of 70 solar flux units, representative of solar minimum conditions (see Figure 3a). The two major peaks seen in the solar flux spectrum are the HeII line at 30.4 nm and the CIII line at 97.7 nm. We would like to point out that the value given for the solar index throughout the paper is that at Earth's orbit.

2.3. Ionospheric Model

[11] On the basis of the thermosphere described in section 2.1, the 1-D ionospheric module solves the equations of ion continuity, momentum, and energy using the methods and rates described by *Moore et al.* [2004] and *Moore et al.* [2008]. Specifically, the ionosphere is solved via explicit time integration, includes a treatment of attenuation of sunlight by the rings of Saturn (not used in this study), and adopts the *Moses and Bass* [2000] treatment of reaction k_1 , the charge exchange between H^+ and vibrationally excited H_2 . The nominal k_1 reaction rate used here is 25%

that of the *Moore et al.* [2004] rate, i.e., $2 \times 10^{-14} \text{ cm}^{-3} \text{ s}^{-1}$ above 2000 km, and ranging from (0.2 to 200) $\times 10^{-16} \text{ cm}^{-3} \text{ s}^{-1}$ below. This reduction is due to two factors: (1) the assertion by *Huestis* [2008] that there may be additional vibrational relaxation of H_2 that has not been accounted for in previous derivations and (2) the fact that a water influx of the magnitude estimated from pre-Cassini era sources [e.g., *Jurac and Richardson*, 2005] is capable of depleting the ionospheric electron density to observed levels [*Moore et al.*, 2006]. In addition, a steady-state influx of water at the top of the atmosphere of $5 \times 10^6 \text{ cm}^{-2} \text{ s}^{-1}$ is used to derive neutral water densities. This flux is within the boundaries of previous estimates [e.g., *Connerney and Waite*, 1984; *Moses et al.*, 2000b], and only accounts for a fraction of the possible geyser source at Enceladus [e.g., *Porco et al.*, 2006]. While the values for both of these loss processes (i.e., the k_1 reaction and the rate of water influx) are within the estimates of our current, best knowledge, they are still under significant debate. As our study is focused on the effects of solar primary and secondary ionization, however, its conclusions are relatively insensitive to the exact combination of those loss processes, and therefore should remain valid should those values be modified in the future.

3. Solar Energy Deposition

3.1. Penetration Altitude of Solar Photons

[12] The penetration altitude of solar photons at a given wavelength is defined as the altitude at which the solar flux at this wavelength has been reduced by a factor e from its value at the top of the atmosphere. It corresponds to an optical depth of unity and is a function of the photoabsorption cross section, total neutral atmospheric density, composition and *sza*. The penetration altitudes derived for 30° *sza* (1200 LT) and 90° *sza* (0600 or 1800 LT) under solar minimum conditions (see Figure 3a) are given in Figures 3b and 3c.

[13] Being the most abundant neutral species in the altitude range studied (600–3000 km), molecular hydrogen is the main absorber below 85.4 nm, the H_2 continuum absorption threshold [*Kim and Fox*, 1994]. In this wavelength window, the spectral shape of the penetration altitude follows that of the H_2 photoabsorption cross section (Figure 2a), that is, monotonically increasing with wavelength. Because of an increasing atmospheric column density with *sza* at a given altitude, the value of the penetration altitude at a given wavelength increases from 30° *sza* to 90° *sza*, as illustrated in Figures 3b and 3c (see also Table 2). Below 75 nm, the penetration altitude at solar local noon (30° *sza*) is in very good agreement with that given by *Moses and Bass* [2000, Figure 2] for similar conditions. Between 75 and 85 nm, the origin of the disagreement is not clear. The spectral shape of the penetration altitude in this wavelength range is primarily controlled by the H_2 photoabsorption cross section. In both studies, this cross section is derived from *Backx et al.* [1976] and does not show any decrease above 75 nm (Figure 2a). Such a decrease would, however, explain the decrease seen in the spectrum of the penetration altitude derived by *Moses and Bass* [2000]. Above ~ 85.4 nm, our estimation of the penetration altitude (grey box) should be taken with caution, as the 1-nm

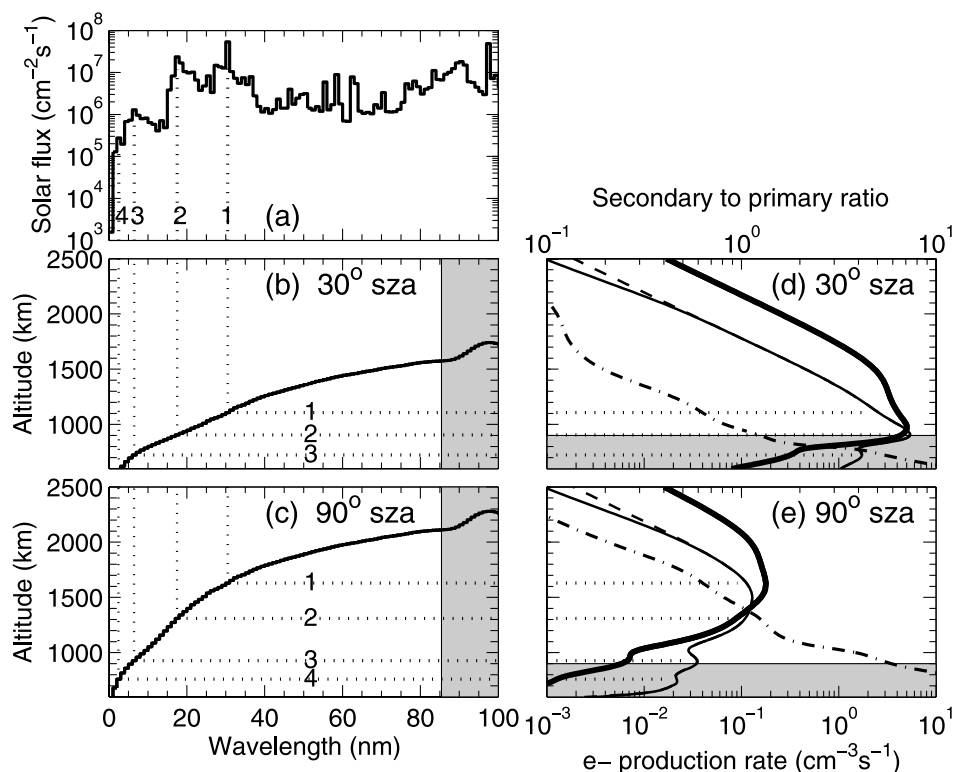


Figure 3. (a) TIMED/SEE solar flux extrapolated to Saturn's location under solar minimum conditions (15 May 2008, with $F_{10.7} = 70$). (b) Penetration altitude of solar photons as a function of the photon wavelength for 30° sza (1200 LT) under solar minimum conditions illustrated in Figure 3a. This altitude corresponds to an optical depth of unity. The penetration altitude in the grey region should be disregarded as our spectral resolution (1 nm) cannot capture the H_2 absorption discrete lines present in this spectral region (see section 3.3). (c) Same as Figure 3b but for 90° sza (0600 or 1800 LT). (d) Primary (thick, solid line) and secondary (thin, solid line) electron production rates for 30° sza (1200 LT). The secondary to primary electron production rate is also shown (dashed-dotted line). The secondary electron production obtained assuming no transport for the suprathermal electrons is shown as a dashed line. Our estimation of the primary electron production rate is underestimated in the hydrocarbon layer (grey box), while the secondary electron production rate is valid throughout the entire altitude region (see section 3.3). As a consequence, the secondary-to-primary ratio is overestimated in the hydrocarbon layer (grey box). (e) Same as Figure 3c but for 90° sza (0600 or 1800 LT). The dotted lines identify four peaks in the solar spectrum, hereafter referred as peaks 1, 2, 3, and 4 (Figure 3a), the corresponding penetration altitudes (Figures 3b and 3c), and the electron production rates at these altitudes (Figures 3d and 3e).

spectral resolution considered here does not allow us to capture the fine structures of the H_2 emissions from the Lyman, Werner, and higher energy band systems.

3.2. Primary Versus Secondary Electron Production

[14] Altitude profiles of the primary (thick solid lines) and secondary (thin solid lines) electron production rates derived from the energy deposition model for 30° sza (1200 LT) and 90° sza (0600 or 1800 LT, that is, at the terminators) are plotted in Figure 3d and 3e, respectively. These results are valid under solar cycle minimum conditions ($F_{10.7} = 70$). The effect of cycle activity on the electron production rates and the sensitivity of the electron production rate to the solar flux model are presented in Appendices A and B, respectively. As discussed in section 3.3, our estimation of the primary electron production rate in the hydrocarbon layer (below ~900 km, identified by the

grey box) is significantly underestimated and thus should be taken with caution, while the secondary electron production rate is valid throughout the altitude region considered.

[15] The ratio of the secondary to the primary electron production rates is shown in dash-dotted lines in Figures 3d and 3e. Because of the underestimation of the primary electron production rate, the ratio is overestimated in the hydrocarbon layer (grey box). The secondary production rate becomes larger than the primary production rate at an altitude corresponding to the penetration altitude of solar photons of wavelength below 20 nm, that is, of energy above ~60 eV. The most probable ionization is the single, nondissociative ionization of H_2 with an ionization threshold energy of 15.4 eV, yielding photoelectrons of energy above 45 eV. The more energetic the solar photons are, the larger the energy of the produced photoelectrons, and

Table 2. Identified Peaks in the Solar Spectrum and Associated Characteristics in Terms of Penetration Altitude z_p and Secondary p_s to Primary p_p Production Rate Ratio^a

| Peak ^b | Wavelength Bin (nm) | z_p^c (km) | | p_s/p_p^d |
|-------------------|---------------------|--------------|---------|-------------|
| | | 0600 LT | 1200 LT | |
| 1 | 30–31 (30.4 HeII) | 1630 | 1110 | 0.6 |
| 2 | 17–18 | 1310 | 905 | 1.2 |
| 3 | 5–6 | 930 | 725 | 5 |
| 4 | 2–3 | 760 | <600 | 17 |

^aNote that solar photons associated with peak 4 penetrate below the bottom altitude boundary, that is, 600 km.

^bSee Figure 3a.

^cSee Figures 3b and 3c.

^dSee Figures 3d and 3e.

therefore, the larger the secondary to primary electron production rate ratio. Keeping in mind the decreasing penetration altitude with decreasing wavelength (below 85 nm), this yields a monotonically increasing ratio with decreasing altitudes (see dash-dotted lines in Figures 3d and 3e).

[16] In order to interpret the shape and relative magnitude of the primary and secondary electron production profiles, we have selected four peaks in the solar spectrum, as illustrated in Figure 3a. The penetration altitudes associated with these spectral peaks and the production rates associated with these altitudes are identified through the dotted lines in Figure 3 with quantitative estimates provided in Table 2. The strong HeII (30.4 nm) line, identified as peak 1, is responsible for the maximum production rate at 90° sza. At 30° sza, it is not the case. Because of the sharp change in gradient of the main constituent, H₂ (see Figure 1 and discussion in section 2.1), the primary electron production rate at the penetration altitude of peak 2 is larger than that corresponding to peak 1 (Figure 3d). The sharp decrease in the solar flux at wavelength shortward of peak 2 induces the sharp decrease in the primary electron production rate seen both at 30° and 90° sza. Peaks 3 and 4 correspond to soft X-ray photons of energy greater than 200 eV. They are responsible for two clear peaks in the secondary electron production rate profile at 90° sza (see Figure 3e). Only one peak is apparent at 30° sza (see Figure 3d), as the penetration altitude of peak 4 at this local time is below the altitude range considered here for the atmospheric model (600 km) (see Figure 3b).

[17] In order to demonstrate the local origin of the suprathermal electrons, we have also computed the electron production rates assuming no transport of the suprathermal electron population. The derived secondary electron production rates are shown in dashed lines in Figures 3d and 3e. There is no significant change in electron production rate between the transport case and the local approximation below 2000 km. In this altitude range, the energetic electrons are primarily produced locally from photoionization and electron-impact ionization.

[18] Figure 4 shows the suprathermal electron spectra in terms of mean intensity at four altitudes chosen to be the penetration altitudes of the four peaks identified in the solar spectrum (see Figure 3a and Table 2). We have selected the 90° sza case, as it allows the inclusion of all four selected spectral peaks. The electron spectrum at a given altitude is driven by solar absorption of most wavelengths shortward of the wavelength of photons whose penetration altitude

corresponds to the altitude of the electron spectrum. For instance, at 1630 km, the penetration altitude of 30–31 nm photons at 90° sza (see Table 2 and Figure 3e), the electron spectrum is driven by absorption of solar photons of wavelength smaller than 31 nm. More specifically, the electron spectrum is the combination of three contributions initiated by solar absorption: (1) production of photoelectrons through ionization of atmospheric neutrals by solar photons, (2) production of secondary electrons by electron-impact ionization of atmospheric species, and (3) energy degradation resulting from the collisions undergone by the suprathermal electrons (photoelectrons and secondary electrons) with atmospheric species (neutrals and thermal electrons). As pointed out in Figure 3e, the energy degradation is primarily local below 2000 km. This means that a photoelectron or a secondary electron produced at a given altitude is going to be thermalized at this same altitude.

[19] Below 15 eV, the energy degradation contribution is dominant and the spectrum intensity is smooth. Above 15 eV, the peaks seen in the spectrum at 1630 km (solid line in Figure 4) are photoelectron signatures. The feature peaking at 25.4 eV well above the mean level is the signature of photoelectrons produced through the single, nondissociative ionization of H₂ by the solar line HeII

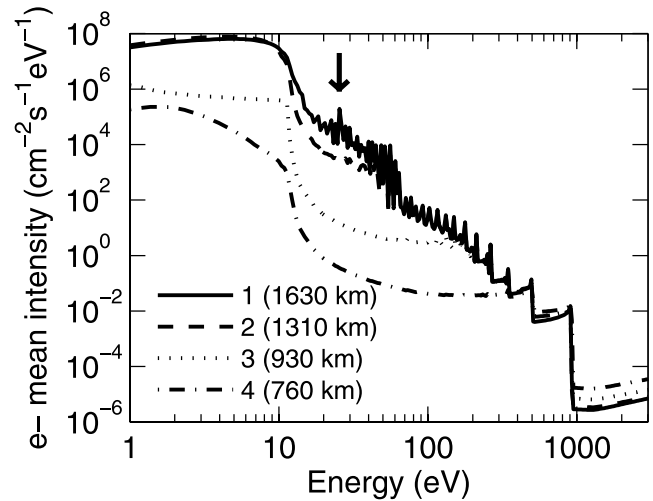


Figure 4. Suprathermal electron mean intensity as a function of electron energy at 90° sza under solar minimum conditions (same as for Figure 3) at four selected altitudes. These altitudes correspond to the penetration altitudes z_p of solar photons associated with the four selected peaks 1 to 4 in the solar spectrum (see Figure 3a and Table 2). The electron spectrum at 1630 km (solid line), 1310 km (dashed line), 930 km (dotted line), and 760 km (dashed-dotted line) is driven by solar absorption of most wavelengths below 31 nm, 18 nm, 6 nm, and 3 nm, respectively. This is a consequence of the monotonic behavior of the penetration profile as a function of solar photon wavelength below 80 nm (see Figure 3c). The vertical arrow identifies the photoelectron peak at 25.4 eV associated with the ionization of H₂ by HeII 30.4 nm solar photons producing H₂⁺. The 1-nm resolution of the solar flux used as input causes the discrete steps that are most obvious for electron energies above 100 eV. It does not, however, affect energy-integrated quantities, such as electron production rates.

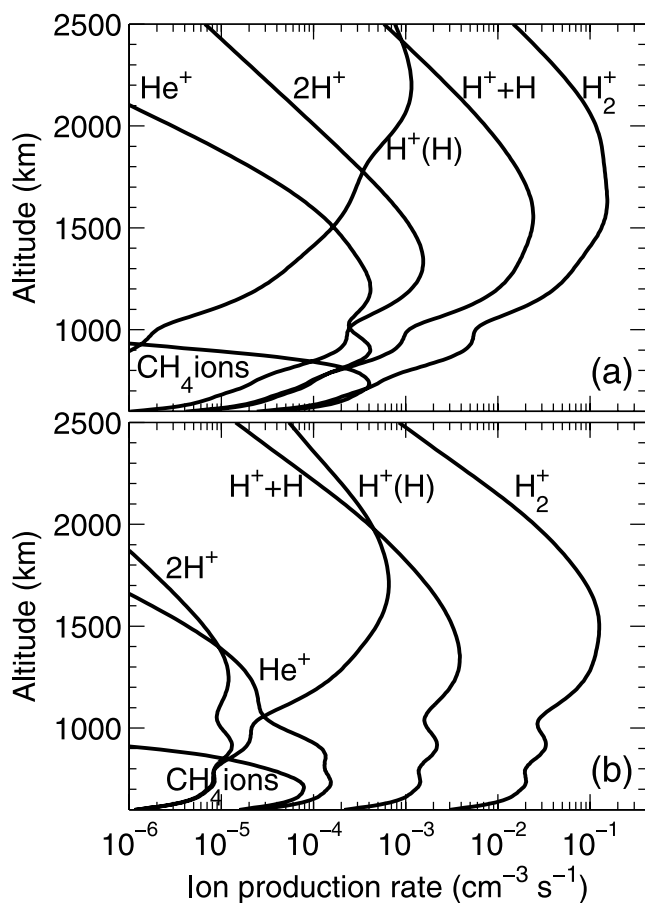


Figure 5. (a) Primary and (b) secondary ion production rates at 90° sza under solar minimum conditions (same as for Figure 3). The profiles labeled H_2^+ , $H^+ + H$, and $2H^+$ are associated with the ionization of H_2 , while the profiles labeled $H^+(H)$ and He^+ are associated with the ionization of H and He , respectively. While the production of each ion species associated with methane is computed individually, taking into account the respective ionization threshold energy and cross section, for clarity only the total production rate is plotted here, with the label CH_4 ions. The CH_4 ions primary rate (Figure 5a) represents a qualitative estimate of the hydrocarbon contribution to primary ion production rates. Our underestimation of the hydrocarbon primary production rates does not, however, affect our estimation of the secondary ion production rates (see text).

(30.4 nm) (identified as peak 1 in Figure 3a). The relevance of this peak and its expected detection by Cassini Plasma Spectrometer (CAPS)/Electron Spectrometer sensor (ELS) are discussed in section 5. In the modeled spectrum the photoelectron peaks are not, however, restricted to the strong solar lines, as in observed spectra. Some are associated with the discretization of the solar flux. The 1-nm resolution of the solar flux causes discrete steps, resulting from the photoelectron peak itself and its associated energy degradation, that are most obvious for electron energies above 100 eV. We have, however, verified that quantities integrated over energy, such as the electron and ion production rates, are not affected by this discretization.

[20] At 1310 km, well below the penetration altitude of the HeII solar line (1630 km), the strong photoelectron signature associated with HeII at 25.4 eV is as expected absent from the electron spectrum (dashed line in Figure 4). The increase in electron mean intensity from 1310 km (dashed line in Figure 4) to 930 km and 760 km (dotted and dash-dotted lines in Figure 4) around 1 keV is associated with the ionization by soft X-ray photons (especially peaks (3) and (4)), which penetrate below 1000 km (see Table 2).

3.3. Ion Production

[21] The altitude profiles of the primary ion production rates are given in Figure 5a for 90° sza under solar minimum conditions. In several aspects they confirm the earlier findings by *Moses and Bass* [2000] and *Moore et al.* [2004]:

[22] 1. The most abundant species produced through photoionization by solar photons below 80.4 nm (the ionization threshold of H_2) is H_2^+ . We found one exception though. At large solar zenith angles, solar irradiance below 5 nm deposits its energy in the hydrocarbon layer (Figure 3c). The low mixing ratio of CH_4 , even in the hydrocarbon layer (Figure 1a), is counterbalanced by the values for the CH_4 photoionization cross section being significantly larger than those of the other neutral species, and the presence of a peak in the solar flux in the 2–3 nm range. As a result, the primary ionization production rate of CH_4 is comparable to the production rate of H_2^+ near 700 km and below (see Figure 5a).

[23] 2. Near and below the primary electron production peak, H^+ is produced mainly through the dissociative photoionization of H_2 , as the result of the relatively low density of H compared with H_2 in this altitude region. However, because of the update of the H_2 photoionization cross section producing $H^+ + H$ (see section 2.2), we find that the direct photoionization by H becomes dominant at higher altitudes than previously predicted, above 2500 km at all sza (below 90°). Though the bottom side of the H^+ profile (from H photoionization) behaves in a similar manner to what was found in previous Saturn studies, a higher spectral resolution would have yielded the extension of the H^+ profile toward lower altitudes because of the absorption of solar photons longward of the H_2 continuum absorption threshold (85.4 nm), as was found at Jupiter [*Kim and Fox, 1994*].

[24] 3. The hydrocarbon ions are confined to below ~ 900 km as a result of the location of the hydrocarbon neutral layer.

[25] 4. Similar to what was found at Jupiter [*Kim and Fox, 1994*], He^+ remains a minor species. The combination of the high ionization threshold energy (24.6 eV corresponding to 50 nm) and the smaller scale height of He relative to H_2 with increasing altitude above the homopause due to higher mass yields a sharp decrease of He^+ photoproduction toward high altitudes. Along with large photoionization cross section values compared with H_2 , this results in a more pronounced peak seen at 930 km, just below the homopause, and associated with the deposition of “peak 3” solar photons (see Figure 3a).

[26] Our estimation of the hydrocarbon primary production rates should be regarded as qualitative. It provides an altitude marker of the contribution of the hydrocarbon species. Only methane, the most abundant and main

absorber among the hydrocarbon species, is included in our simulations and the spectral resolution considered is that commonly provided by the solar flux models, that is, 1 nm. As a result, the primary electron production rate below about 900 km where the hydrocarbon layer is present, is significantly underestimated. The reason is twofold. (1) While hydrocarbon species are minor constituents of Saturn's thermosphere, they are ionized above 91.2 nm, a spectral region where H₂, H, and He (with an ionization threshold of 80.4 nm, 91.2 nm, and 50.4 nm, respectively) no longer undergo ionization. CH₄ is ionized up to 99 nm and CH₃ up to 126 nm. The latter includes the contribution of the strong solar H Lyman α line (121.6 nm) which penetrates down to the hydrocarbon layer and yields significant photoionization rates for CH₃ [Moses and Bass, 2000]. (2) Above about 85.4 nm, H₂ absorbs in discrete transitions through the Lyman, Werner, and higher energy band systems. In order to capture these fine structures, a very high spectral resolution is needed. Kim and Fox [1991] carried out calculations with a 10⁻⁴ nm resolution at Jupiter and found that two strong solar lines (CIII at 97.7 nm and OVI at 103.2 nm) and 30% of the continuum solar flux between 91.2 nm and 111.6 nm penetrate below the methane homopause. This yields significant photoionization rates for methane, acetylene, ethane, and ethylene [Kim and Fox, 1991, 1994]. Similar sources of photoionization are expected at Saturn [Moses and Bass, 2000], but calculations of solar deposition at such a very high spectral resolution have not yet been carried out at this planet.

[27] The secondary ion production rates are plotted in Figure 5b for 90° sza under solar minimum conditions. As H₂ is the dominant neutral species, H₂⁺ is found to be the major ion species produced through electron impact. Even though electron-impact ionization cross sections of methane are more than three times larger than those of molecular hydrogen, the low methane mixing ratio yields an ionization rate more than two orders of magnitude lower than that of H₂⁺ over all sza under sunlit conditions. The H₂⁺ secondary production rate is larger than the primary production at altitudes below the penetration altitude of 20 nm solar photons, in agreement with electron production rate results (see section 3.2). This region corresponds to the production of photoelectrons of energy above about 45 eV, efficient ionizers. The combination of low neutral density and of ionization cross sections lower than those of molecular hydrogen yields a production rate for He⁺ two orders of magnitude lower than that of H₂⁺ below the homopause and more than two orders of magnitude above. Just as with primary production, H⁺ ions are primarily produced by dissociative ionization of H₂ near and below the peak of the total ion production rate. Direct ionization of atomic hydrogen becomes important above 2000 km under sunlit conditions independent of the sza. It should be noted that the underestimation of the primary ion production rates associated with hydrocarbons and discussed earlier in this section does not affect the secondary ion production rates. The contribution currently neglected is primarily associated with the ionization by solar photons above 91.2 nm (corresponding to an energy of 13.6 eV). The induced photoelectrons do not have enough energy to ionize a neutral species. In addition, as the hydrocarbon neutral mixing ratios are very small [Moses and Bass, 2000], the

direct electron-impact ionization of the hydrocarbon neutrals is negligible compared with the H₂ secondary production rate.

4. Contribution of Secondary Ionization to the Ionospheric State

4.1. Solar Minimum

[28] The prime focus in this section is the contribution of suprathermal electrons to ionospheric densities. While the electron density peak region is in photochemical equilibrium, plasma diffusion at higher altitudes becomes an increasingly important process, controlling the upper part of Saturn's ionosphere (≥ 2300 km) [Moore et al., 2004]. The electron density as a function of altitude and local time is shown in Figure 6 (top), for the same conditions as for Figure 3, that is, using the TIMED/SEE solar flux from 15 May 2008, representative of solar minimum conditions ($F_{10.7} = 70$). The altitude profile of key ion species at three selected times (sunrise (90° sza), noon (30° sza), and sunset (90°)) are plotted in Figure 6 (bottom). The general diurnal behavior of Saturn's ionosphere with H⁺ and H₃⁺ as the major ions above the homopause exhibits similar characteristics as previously found and explained [Moses and Bass, 2000; Moore et al., 2004, 2006, 2008].

[29] Figure 7 shows the ratio between the electron density from Figure 6 and the electron density from an identical run but with no contribution from suprathermal electrons. In the latter case, the electron and ion production rates are reduced to primary production and the electron temperature is equal to the neutral temperature. As pointed out by Moore et al. [2008], the increase in electron temperature due to heating by suprathermal electrons does not strongly affect the chemistry. Therefore, the ratio in Figure 7 primarily highlights the contribution of secondary ion production to the electron density profiles. Secondary ion production becomes significant below 1500 km at sunrise and sunset and below 1000 km at local noon (see section 3). This corresponds to the region at and below the ionospheric peak. In this region, H₂⁺ is the major ion produced through secondary production by far (see Figure 5). Through charge-exchange reactions of H₂⁺ with H and H₂, secondary production indirectly affects H⁺ and H₃⁺ in this altitude region. At noon, secondary ion production increases the electron density at the ionospheric peak by 30% (ratio of 1.30), reaching a value of $9.3 \times 10^3 \text{ cm}^{-3}$. It also shifts the peak toward lower altitudes from 1380 km down to 1060 km. While the former is a result of combined H⁺ and H₃⁺ profiles, the latter corresponds to the peak in H₃⁺ density, which builds faster than H⁺ density. This results from the fact that the loss of H₂⁺ producing H₃⁺ is faster than that producing H⁺. The largest increase above the homopause is found at 0700 LT, just after sunrise at a time when the H₃⁺ density is building up very fast. At that time, H₃⁺ represents 75% of the ion density at 1000 km and the electron density increases by a factor of 2.6 because of secondary production, reaching $1.1 \times 10^3 \text{ cm}^{-3}$. After sunset, even though the secondary production is off, the effect on the electron density can still be seen because of the long lifetime of H⁺ affected by the secondary production before sunset.

[30] Below the homopause, H₂⁺ ions are converted to complex hydrocarbons. Though our quantitative estimation

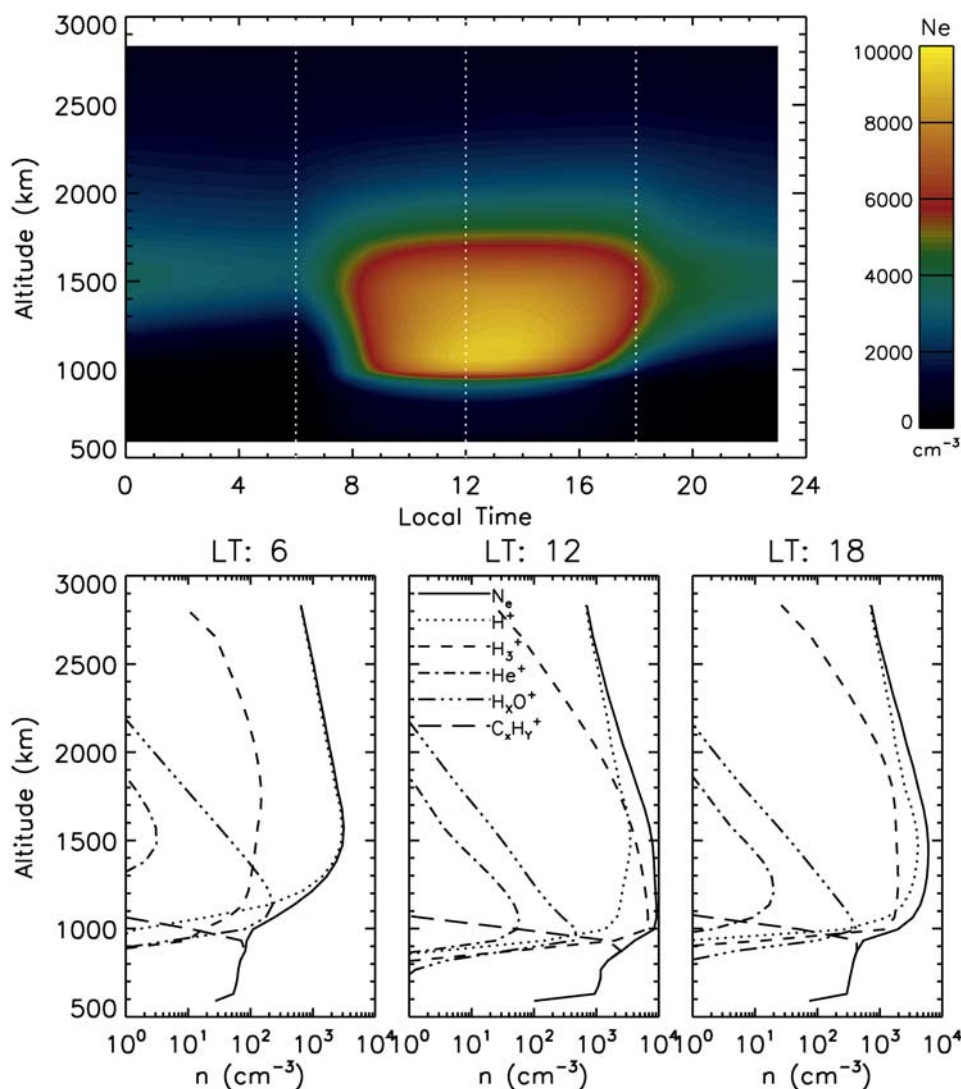


Figure 6. (top) Color plots of the electron density as a function of local time and altitude under solar minimum conditions (15 May 2008, with $F_{10.7} = 70$). The white, dotted lines indicate the time at which the altitude profiles given in the bottom have been extracted. Secondary electron and ion production has been taken into account in the ionospheric calculations. (bottom) Profiles in altitude of the densities of the electrons and major ion species (left) at sunrise (0600 LT), (middle) at local noon, and (right) at sunset (1800 LT).

of electron density is limited in this region, we are calculating the secondary production rates in a rigorous manner (see section 3.3) and find that H_2^+ secondary rate is larger than five times the H_2^+ primary rate at all local times at 700 km. Extrapolating from the ionospheric calculations of *Moses and Bass* [2000] based only on primary ion production rates but with the full, complex hydrocarbon chemistry, we are able to demonstrate a significant effect of secondary production on the electron and ion densities in the hydrocarbon layer and confirm the earlier predictions by *Moses and Bass* [2000].

4.2. Variability With Solar Activity

[31] For the solar maximum calculations we assume the same neutral atmosphere as used for the solar minimum case (see Figure 1). As yet it is unclear from measurements by how much the neutral densities change with solar cycle.

During solar maximum conditions the effects of supra-thermal electrons on Saturn's ionosphere are similar to those at solar minimum (see section 4.1) and are therefore not shown here. The electron density at the peak at noon is increased by 25% (ratio of 1.25) and its altitude decreases from 1380 to 1135 km where it is still the combination of H_3^+ and H^+ profiles.

[32] The electron density ratio between solar maximum conditions (see Appendix A) and solar minimum conditions (see section 4.1) is shown in Figure 8. It highlights the effect of solar activity on the electron density. In the peak region under solar illumination, the electron density peak which is primarily driven by solar EUV irradiation is increased by more than 60% (ratio of 1.60) from solar minimum to solar maximum, while it increases by more than 100% (ratio of 2) because of solar activity between midnight and sunrise. The larger increase found during the night is associated with the

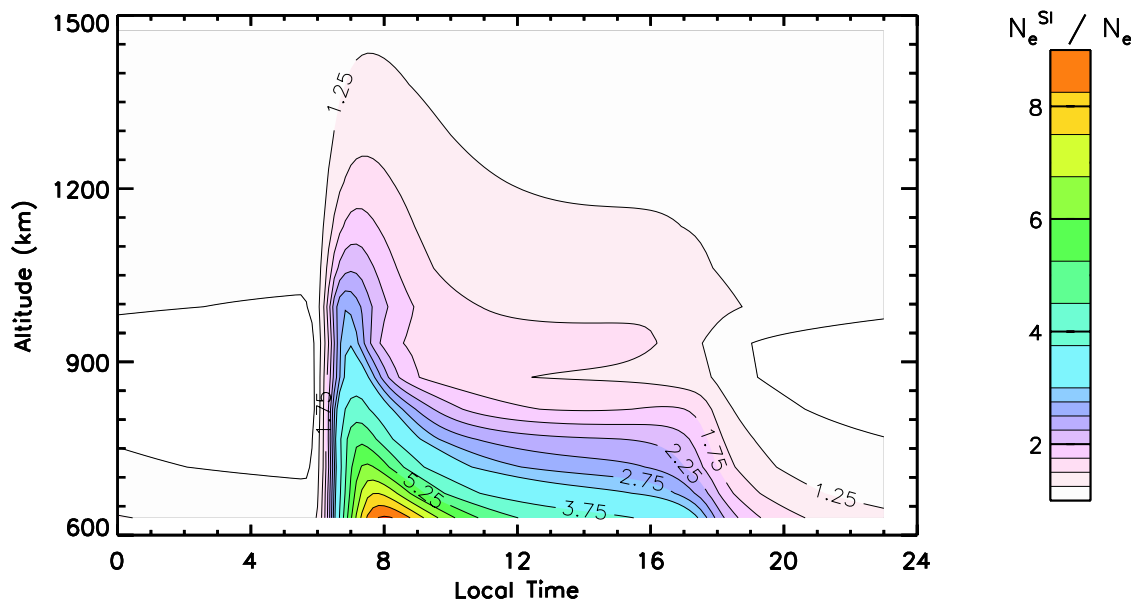


Figure 7. Contour plot as a function of local time and altitude of the electron density ratio between a run including secondary production (see Figure 6) and a run ignoring secondary production as a source term in the continuity equations of the ions. Both runs are valid for solar minimum conditions (15 May 2008, with $F_{10.7} = 70$).

nonlinearity of the loss processes. The largest increase in electron density with solar activity occurs in the region of deposition of soft X rays which is located below the homopause between 0600 and 0800 LT. This is due to the fact that the ratio of solar flux for solar maximum to solar minimum is larger in the X ray than the EUV (see Appendix A).

5. Concluding Remarks and Discussion

[33] The goal of this paper is to assess the importance of solar photoelectrons as a source of ionization of Saturn's

ionosphere and to quantify their contribution to the diurnal, ionospheric structure. We have self-consistently coupled an energy deposition model with an ionospheric model and applied it to midlatitude conditions (30°N) (see section 2). The season was assumed to be equinox and the solar irradiance was taken to be representative of quiet Sun in order to provide conditions similar to those currently encountered by the Cassini spacecraft. The exchange of physical quantities between both models was applied until convergence was reached.

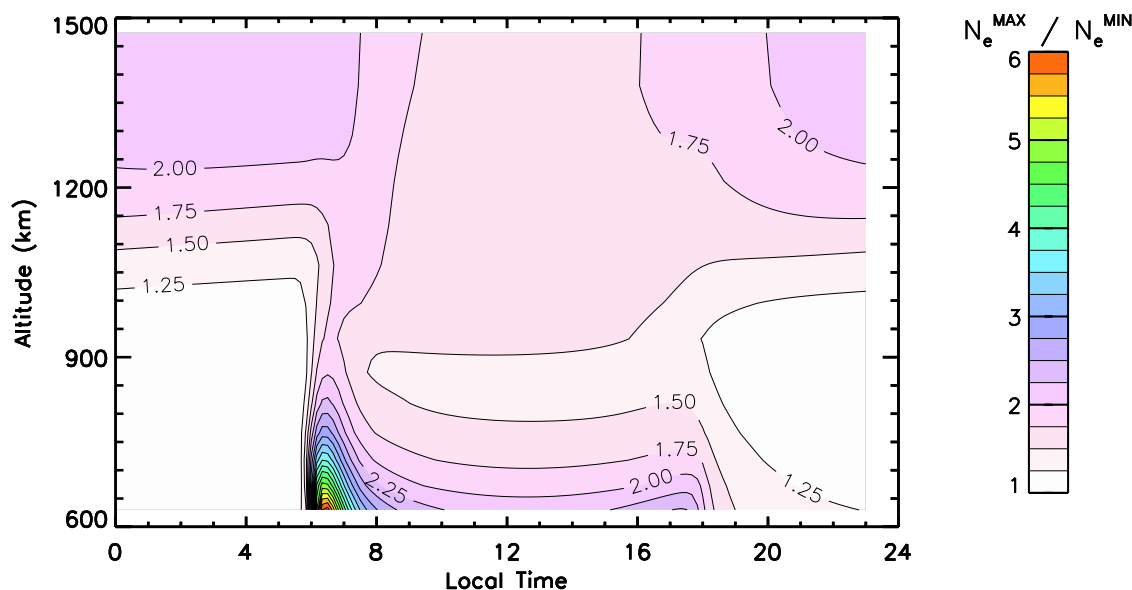


Figure 8. Contour plot as a function of local time and altitude of the electron density ratio between solar maximum conditions (20 October 2002, with $F_{10.7} = 180$) and solar minimum conditions (15 May 2008, with $F_{10.7} = 70$). Secondary electron and ion production has been taken into account in the ionospheric calculations.

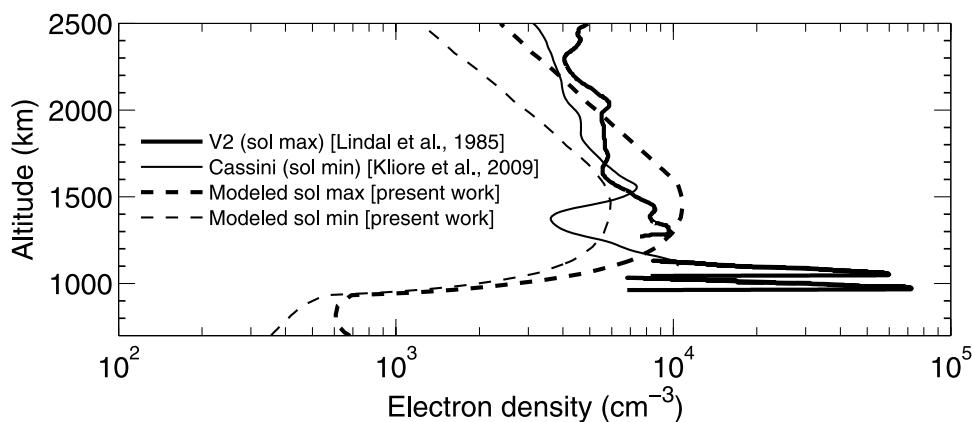


Figure 9. Dusk, midlatitude electron density observed under solar maximum conditions by Voyager 2 ($F_{10.7} = 267$) (thick, solid lines) [Lindal *et al.*, 1985] and under solar minimum conditions by Cassini ($F_{10.7} = 67$) (thin, solid lines) [Kliore *et al.*, 2009]. The modeled electron density at a $z_{\text{sza}} = 90^\circ$ at dusk is plotted in dashed lines for the solar maximum ($F_{10.7} = 180$; see section 4.2) (thick line) and for the solar minimum ($F_{10.7} = 70$; see section 4.1) (thin lines) cases.

[34] The electron and ion production induced by the photoelectrons (and their secondaries) becomes significant at and below the ionospheric peak. As predicted by Moses and Bass [2000] on the basis of an extrapolation from Jovian estimations by Kim and Fox [1994], this electron and ion production yields a significant increase in the ionospheric densities in the bottom side of the ionosphere. We found, however, that the contribution of suprathermal electrons on the ionospheric densities extends toward higher altitudes than originally anticipated. Suprathermal electrons increase the electron peak density by up to 30% (ratio of 1.3) at solar minimum (see section 4.1). Around midday, the altitude of the ionospheric peak is also affected, decreasing by more than 300 km at solar minimum and by about 250 km at solar maximum. The largest contribution above the homopause is found after sunrise below the ionospheric peak with an increase in electron density by a factor of 2.6 at 1000 km at 0700 LT. The suprathermal electrons originating from the absorption of solar photons contribute to the ionospheric structure of Saturn's ionosphere and should be taken into account as a source of ionization when interpreting the observed electron density profiles.

[35] Figure 9 shows a comparison of observed dusk midlatitude electron density profiles between solar maximum conditions (thick, solid line) and solar minimum conditions (thin, solid line). The solar maximum profile is from the ingress radio occultation profile of Voyager 2 taken at a latitude of 36.5°N , a $F_{10.7}$ solar index of 267 at 1 AU and a solar zenith angle of 87° [Lindal *et al.*, 1985]. The solar minimum profile is an average of five profiles from Cassini/RSS occultations, four in the northern hemisphere and one in the southern, with absolute latitude ranging between 28° and 47° , $F_{10.7}$ solar indices ranging between 66 and 68 and solar zenith angles between 83° and 92° [Kliore *et al.*, 2009]. As expected, solar maximum electron density values are overall larger than the solar minimum values. However, the shapes of the two profiles are surprisingly different. In particular, the solar minimum profile shows a bite-out near 1400 km, while the solar maximum profile exhibits a double peak in this region. While the

origin of the bite-out is still uncertain, it could be associated with a time-variable water influx [e.g., Moore *et al.*, 2006; Moore and Mendillo, 2007] or a low-altitude layer of meteoritic origin combined with vertical transport of plasma at high altitude by either neutral winds or electric fields [Moses and Bass, 2000]. In addition, two sharp layers near 1000 km can be seen in the solar maximum profile. Their origin is also uncertain, but they could be attributed to the effect of atmospheric gravity waves, combined if necessary with a sporadic metal ion layer of meteoritic origin, as shown for Saturn [Moses and Bass, 2000] and Jupiter [Matcheva *et al.*, 2001].

[36] In Figure 9 we also show the solar minimum and solar maximum modeled dusk profiles for a solar zenith angle of 90° . They are in general agreement with the observations near the peak, especially considering the slightly different Sun-Saturn distances and solar fluxes. Vertical structuring seen in the observed profiles is not expected to be reproduced by the simulations, as they do not include any processes that would generate such sharp layers. The main purpose of this paper is to assess the importance of photoelectrons as an ionization source, not to reproduce the observations in detail. While the photoelectrons affect the ionospheric structure above 1000 km as mentioned above, the region where their contribution is the largest is below, where it becomes difficult to infer reliable ionospheric densities from the Cassini RSS measurements (A. Kliore, personal communication, 2008).

[37] In order to take the contribution of photoelectrons as a source of ionization into account in general circulation models, such as that developed by Mueller-Wodarg *et al.* [2006], Moore *et al.* [2009] described a parameterization of the electron and ion production rates based on the present study. They discuss the validity of this parameterization, as well as the validity of the parameterization developed for the thermal electron heating rate based on the work of Moore *et al.* [2008], for different latitudes, seasons, and levels of solar activity. These parameterizations are going to be critical, especially for the assessment of the global ionospheric energy budget and ionospheric structure and

composition in Saturn's upper atmosphere. They will also be relevant for deriving quick estimates of the total ionospheric densities for comparison with RSS observed profiles, without the need to solve the full suprathermal electron transport equation.

[38] With H_2 as the main absorber below 85.4 nm (continuum absorption threshold), our estimation of H_2 primary ionization production rates is rigorous throughout this spectral region. However, the primary hydrocarbon ion production rates, significant below ~ 900 km, are underestimated because the fine structures in H_2 photoabsorption have not been taken into account and the hydrocarbon species have been reduced to methane (see section 3.3). The chemistry involving hydrocarbon species is also limited (see section 2.3). As a consequence, the electron and ion (especially hydrocarbon) densities below the homopause should be treated as qualitative. The calculation of the secondary ion production rates provided in the present study is valid throughout the ionospheric region considered, extending from 600 to 3000 km above the 1-bar level (see section 3.3). The secondary production becomes larger than the primary production below the altitude of penetration of solar photons of wavelengths shortward of 20 nm. As a result, the profile in altitude of the secondary production rate is strongly driven by the shape in the solar flux spectrum below this wavelength. The presence of a peak in the solar spectrum yields a peak in altitude for the secondary production rates (see section 3.2). It is therefore critical to have an estimate as good as possible of the highly variable soft X-ray solar flux (see Appendix A). The choice of the solar flux models is critical for assessing ionospheric densities, especially at and below the main peak (see Appendix B). The uncertainty in the solar flux is a limitation in ionospheric models.

[39] Below 85 nm, the penetration altitude decreases with decreasing wavelength of the solar photons (see Figures 3b and 3c). As the solar flux penetrates deeper and deeper in the atmosphere, the EUV range of solar photons which have been fully absorbed is increasing while the soft X-ray photons are reaching lower altitudes. This means that the solar flux becomes more and more energetic, yielding the relative increase in production of photoelectrons having enough energy to ionize in their turn. As a result, the secondary to primary electron production rate ratio increases with decreasing altitude (see Figures 3d and 3e). Below 2000 km, the freshly produced photoelectrons lose locally all of their energy through collisions with atmospheric neutrals and electrons (see section 3.2). Out of the total energy available from the photoelectrons, 20% is used to heat the ionospheric, thermal electrons, yielding an increase in electron temperature above the neutral temperature level in the upper ionosphere [Moore et al., 2008, 2009]; 70–75% is used through collisions with H_2 , including 35% (of the total energy available from the photoelectrons) used to ionize H_2 , yielding an increase in electron density up to 30% at the peak. Near dawn and dusk, more than 5% of the original energy of the photoelectrons leaves the atmosphere, being carried by outgoing electrons. At local noon, this percentage is reduced to 0.4%.

[40] By analogy with auroral particle precipitation [e.g., Rees, 1989], we have estimated the average energy loss per electron produced for the photoelectrons. It is derived from

the ratio between the energy deposition rate of the photoelectrons and the secondary electron production rate. Instead of integrating over altitude, the energy loss is calculated as a function of altitude, each altitude considered being associated with a wavelength of solar irradiance through the penetration altitude function (see Figures 3b and 3c). Such an approach applied to wavelength below 35 nm is justified, as the local approximation is valid at the penetration altitude of solar photons of this wavelength range (see section 3.2). We derive an energy loss per electron produced ranging from less than 30 eV at 1 nm to 50 eV at 35 nm. A parameterization is provided in Table 3. The energy loss is found to be insensitive to local time, as long as there is solar illumination. It is also found to be not significantly dependent on solar activity. Therefore, the parameterization in Table 3 can be used under the whole range of solar activity. The secondary production rate can be derived by dividing the energy flux carried by photoelectrons at this altitude (easily estimated from the Beer-Lambert law) by the energy loss at the wavelength of solar photons whose penetration altitude corresponds to this altitude. The parameterization discussed here does not replace that proposed by Moore et al. [2009], as it does not provide any information on the different ion production rates, even though in first approximation it is justified to reduce the secondary ion species to H_2^+ . It illustrates, however, the different behavior of photoelectrons compared with auroral particles for which a constant energy loss over energies has been derived. A value of 30 eV has been estimated for auroral electrons of energies below 1 keV in a pure H_2 atmosphere [Hiraki and Tao, 2008], while a value of 37 eV has been used for auroral electrons and protons in hydrogen-dominated atmospheres [e.g., Gérard and Singh, 1982; Régo et al., 1994]. While these values are of the same magnitude as those we derived, the strong variability with solar wavelength is not captured. Ignoring this variability would yield an overestimation of the secondary electron production rate at high altitude (above the penetration altitude of solar photons of 3 nm for a value of 30 eV and of 14 nm for a value of 37 eV) and an underestimation at low altitudes (below the penetration altitude of solar photons of 12 nm for a value of 37 eV).

[41] The strong feature peaking at 25.4 eV above the neighboring level in suprathermal electron mean intensity, present in the solid line curve in Figure 4 and identified with a vertical arrow, is the signature of photoelectrons produced through the single, nondissociative ionization of H_2 by the solar line HeII (30.4 nm) (identified as peak 1 in Figure 3a). Such a signature has been unambiguously identified on the observed spectra within the ionosphere of several bodies, such as Earth [e.g., Richards and Torr, 1985, 1988; Solomon et al., 2001] and Titan [Galand et al., 2006], even though at a different energy (24.1 eV), as these bodies have an atmosphere primarily made of nitrogen. Even though the CAPS/ELS instrument onboard Cassini measures suprathermal electron intensities over this energy range, no in situ measurements, and thus no detections, have been made so far in Saturn's dense ionosphere. It may, however, happen during the last phase of the Cassini mission with orbits penetrating into Saturn ionosphere. We also found that the photoelectron signature at 25.4 eV is clearly seen in the suprathermal modeled spectra escaping the atmosphere. We therefore predict that CAPS/ELS should observe this

Table 3. Average Energy Loss per Electron Produced, E_e , at a Given Altitude Representing the Penetration Altitude of Solar Photons of Wavelength λ^a

| λ (nm) | E_e (eV) |
|----------------|------------|
| 1 | 29.0 |
| 5 | 32.1 |
| 9 | 33.5 |
| 13 | 37.5 |
| 19 | 40.2 |
| 26 | 45.2 |
| 30 | 47.0 |
| 32 | 48.5 |
| 35 | 50.0 |

^aThis parameterization is valid from 1 nm to 35 nm, which corresponds to a ratio of secondary over primary electron production rates of 43 down to about 0.5, respectively. A linear interpolation should be applied between two successive points.

signature from the magnetosphere of Saturn at locations where magnetic field lines are connected with the sunlit Saturn ionosphere. Similar observational configurations have allowed the detection of the analog signature at Earth at distances up to 7 Earth radii [Coates *et al.*, 1985].

Appendix A: Variability With Solar Activity

[42] In order to assess the effect of solar variability on the electron production rates, we have selected another day of study, 20 October 2002, which corresponds to solar cycle maximum conditions ($F_{10.7} = 180$). The solar variability between this solar maximum case and the solar minimum default case ($F_{10.7} = 70$) is plotted in Figure A1a. The derived primary (solid) and secondary (dashed) electron production rates at solar maximum (thick lines) and solar minimum (thin lines) for 90° sza are given in Figure A1b.

[43] Saturn was closer to the Sun in October 2002 (solar maximum case) than in May 2008 (solar minimum case). This yields a 6% baseline increase in the solar flux from the solar minimum case to the solar maximum case. However, it is significantly smaller than the variability in the solar flux due to the solar activity alone. Over the entire spectral range considered the solar variability is at least 20% and, for most spectral bins, above 50%.

[44] As expected, the derived solar variability between October 2002 (solar maximum) and May 2008 (solar minimum) is significantly larger in the soft X rays (reaching up to 30) than in the EUV, where the averaged solar variability is of the order of 100% (see Figure A1a). Because of the wavelength dependence of solar variability, the electron production rate is affected significantly more in the lower ionosphere (where soft X-ray photons deposit their energy) than higher up at the penetration altitudes of the solar EUV (see Figures A1b and A1c). At the main peak of the primary electron production located in the solar EUV penetration region (1625 km), the primary production rate increases by a factor of 2.3 at 90° sza (sunrise/sunset) and by a factor of 2.2 at 30° sza (local noon). The secondary electron production rate increases by a factor of ~ 2.4 or less, above 1000 km at 0600 LT and above 800 km at 1200 LT. In the region of solar soft X-ray penetration altitudes, the increase in primary and secondary production

rates becomes larger and larger with decreasing altitude. At 700 km, the primary production rate increases by a factor of 11 at 90° sza and of 2.8 at 30° sza, while the secondary increases by a factor of 13 at 90° sza and of 3.1 at 30° sza. The difference found in the percentage of increase with sza is due to the different wavelength values associated with a penetration altitude of 700 km (see Figures 3b and 3c).

[45] It should be noted that the solar variability exhibits several peaks in the EUV window, in particular around 61 nm (see Figure A1a). Such a peak is of instrumental origin associated with abnormal values in the 60–61 and

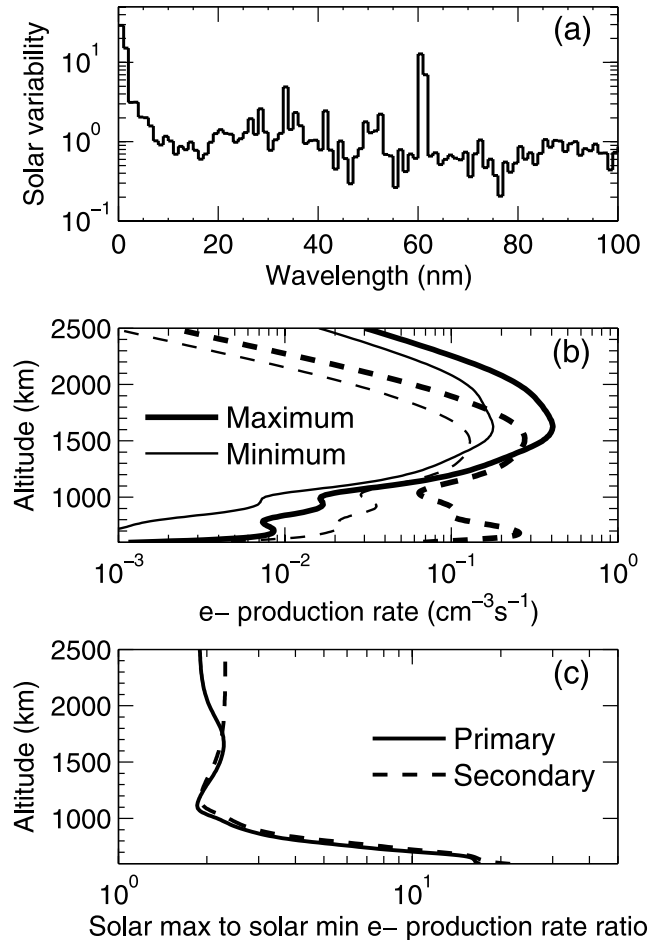


Figure A1. (a) Solar variability between solar cycle maximum (20 October 2002, with $F_{10.7} = 180$) and solar cycle minimum conditions (15 May 2008, with $F_{10.7} = 70$) based on TIMED/SEE observations. The variability is defined as the solar flux ratio between solar maximum and solar minimum minus one, that is, the relative variation. (b) Primary (solid, thick lines) and secondary (dashed, thick lines) electron production rates at 90° sza under solar cycle maximum conditions. For reference, the primary and secondary electron production rates under solar cycle minimum conditions are shown in thin, solid and thin, dashed lines, respectively. (c) Ratio of the electron production rate for solar cycle maximum (20 October 2002) to solar cycle minimum (15 May 2008). Primary production rate ratio and secondary production rate ratio are shown in solid and dashed lines, respectively.

61–62 nm bins of the solar flux from the recent solar minimum data set (version 9 TIMED/SEE) (T. Woods, personal communication, 2008). In order to test the sensitivity of our solar minimum results to this feature, we have run the model with a solar minimum flux modified in the 60–62 nm range such that the solar variability in this range is 0.7, typical of the neighboring spectral region. The inferred primary production rate is affected by less than 7% in the upper part of the ionosphere above the penetration altitude of 60 nm (see Figures 3b and 3c). The secondary electron production rate is not changed, as photoelectrons produced by solar photons of 60 nm (or 21 eV) do not have enough energy to ionize the neutral species. The effect of the too low solar minimum values near 60 nm is therefore negligible.

[46] While the analysis presented in this section is based on two specific days, it is representative of a typical solar cycle variability. We have extracted the solar flux for different days associated with similar $F_{10.7}$ levels. At solar cycle maximum, the variability from the level obtained on 20 October 2002 is within $\pm 20\%$, and decreases to $\pm 10\%$ above 60 nm. At solar cycle minimum, the variability from the level on 15 May 2008 is within $\pm 10\%$ over the whole spectral range. The only exception is in the soft X rays where specific events, such as solar flares, can be associated with fluxes several orders of magnitude above the “quiet Sun” level [e.g., *Neupert, 2006*].

Appendix B: Sensitivity to Solar Flux Models

[47] The altitude profiles of the primary and secondary electron production rates are strongly dependent on the solar flux spectrum considered to drive the model. This is especially true in the soft X-ray range which drives significant secondary production peaks in the lower ionosphere. The solar flux spectrum that we are using is based on the TIMED/SEE observations made from Earth and averaged over one day (see section 2.2). Other solar empirical models have been used by the aeronomy community. For instance, the solar EUV flux model for aeronomic calculations (EUVAC) driven by the daily solar index, $F_{10.7}$, was developed by *Richards et al. [1994]*. Figure B1a shows the primary and secondary electron production rates for 90° sza derived from the EUVAC model with $F_{10.7} = 180$ (thick lines) and from TIMED/SEE under solar maximum conditions as defined in Appendix A (thin lines). At the penetration altitude of the solar EUV irradiance (see Figure 3c), the primary production rates are in very good agreement. The prime difference between EUVAC and the TIMED/SEE models is associated with the lower spectral boundary set to 5 nm in the EUVAC model, while the smallest spectral bin for TIMED/SEE is 0–1 nm. As a result, both the primary and secondary electron production rates sharply fall off at an altitude significantly larger than the altitude predicted when using a solar flux extending toward lower wavelengths. This highlights once more the role solar soft X-ray irradiance plays in the low ionosphere as a source of ionization.

[48] Figure B1a also shows that the production rates derived from EUVAC have significantly larger values above the sharp fall off than those derived from TIMED/SEE. The

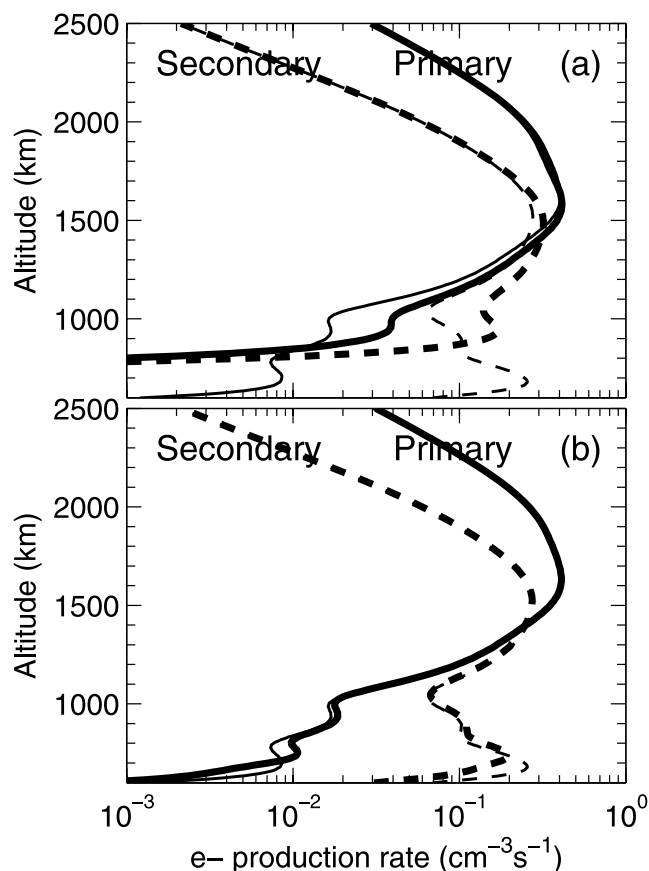


Figure B1. Primary (thick, solid lines) and secondary (thick, dashed lines) electron production rates at 90° sza under solar maximum conditions with the solar flux generated (a) with the EUVAC model and (b) with the Solar 2000 model version 2.34. For reference, the primary and secondary electron production rates under solar maximum conditions based on TIMED/SEE are shown in thin, solid and thin, dashed lines, respectively.

reason is the larger values for the solar flux in the 5–10 nm range for EUVAC compared with TIMED/SEE. While the $F_{10.7}$ solar index and its 81-day average which drive the EUVAC model are good proxy for the EUV solar flux, they cannot capture the variability in the soft X rays, which is significantly greater than that in the EUV. Recently, *Richards et al. [2006]* published a high-resolution version of the solar EUV irradiance for aeronomic calculations (HEUVAC) which extends down to 0.1 nm and provides an update of the EUVAC model. In particular, they introduce an additional solar activity scaling factor over 0–5 nm window, making the solar irradiance in this range vary by a factor of six when the proxy for EUV ($F_{10.7} + F_{10.7}(81\text{-day average})/2$) goes from 80 to 200. This partially addresses the soft X-ray contribution and its variability over the solar activity, both absent in the previous EUVAC version.

[49] Another solar flux model commonly used is the Solar 2000 model [*Tobiska, 2004; Tobiska and Bouwer, 2006*]. The most recent version, v2.34, is primarily based on the observations of the daily TIMED/SEE. It is therefore not

surprising that the electron production rates derived from Solar 2000 v2.34 are very close to those derived from TIMED/SEE, as illustrated in Figure B1b valid for solar maximum conditions (20 October 2002) at 90° sza. In the soft X rays, the Solar 2000 v2.34 provides a flux value 55% smaller (ratio of 0.45) in the 1–2 nm bin and a factor of 2.6 larger in the 2–3 nm bin, compared with TIMED/SEE. These differences yield more than a 40% decrease (ratio of 0.6) for the primary and secondary production rates at the penetration altitudes of 1–2 nm (680 km) and 40% increase (ratio of 1.4) in the primary and 20% increase (ratio of 1.2) in the secondary electron production rates at the penetration altitudes of 2–3 nm (760–790 km).

[50] Earlier versions of the Solar 2000 model provide very different results in terms of electron production rates. For instance, if the v1.24 version would have been used instead of the v2.34, the solar flux would have been more than three orders of magnitude lower in the 2–3 nm bin and more than one order of magnitude larger in the 3–4 nm bin (ratio of 22) and in the 12–13 nm bin (ratio of 17). Using v1.24 compared with v2.34 yields an increase of five times the primary production rate and by an order of magnitude of the secondary production rate at the penetration altitude of 12.5 nm solar irradiance. The choice of the solar flux models (and of its versions) is critical for aeronomical studies. The uncertainties in the solar flux, especially in the soft X rays, is a strong limitation factor of the estimation of ionospheric conditions.

[51] **Acknowledgments.** This work was supported, in part, by a grant from the NASA Cassini Data Analysis Program (CDAP) and the Planetary Atmospheres Program to Boston University. M.G. was partially supported by the Science and Technology Facilities Council (STFC) rolling grant to Imperial College London. We would like to thank the Cassini/RSS PI, Arv Kliore, who kindly provided us with the midlatitude electron density profiles. We are also very grateful to the TIMED/SEE PI, Tom Woods, and his team for providing us with the solar flux data set, associated routines of extrapolation to planets, and constructive insight on the solar data set (<http://lasp.colorado.edu/see/>). SOLAR2000 Research Grade historical irradiances are provided courtesy of W. Kent Tobiska and SpaceWx.com. These historical irradiances have been developed with funding from the NASA UARS, TIMED, and SOHO missions. We would like to thank Hannelore Keller-Rudek and Geert K. Moortgat for making available to the scientific community the MPI-Mainz-UV-VIS Spectral Atlas of Gaseous Molecules (<http://www.atmosphere.mpg.de/spectral-atlas-mainz>). This database has been used for the update of the H₂ photoabsorption cross sections.

[52] Zuyin Pu thanks Thomas Woods and another reviewer for their assistance in evaluating this paper.

References

- Ajello, J. M., D. E. Shemansky, and G. K. James (1991), Cross sections for production of H (2p, 2s, 1s) by electron collisional dissociation of H₂, *Astrophys. J.*, *371*, 422–431, doi:10.1086/169904.
- Atreya, S. K., and T. M. Donahue (1975), Ionospheric models of Saturn, Uranus, and Neptune, *Icarus*, *24*, 358–362.
- Atreya, S. K., J. H. Waite, T. M. Donahue, A. F. Nagy, and J. C. McConnell (1984), Theory, measurements and models of the upper atmosphere and ionosphere of Saturn, in *Saturn*, edited by E. Gehrels, pp. 239–277, Univ. of Ariz. Press, Tucson.
- Backx, C., G. R. Wight, and M. J. Van der Wiel (1976), Oscillator strengths (10–70 eV) for absorption, ionization, and dissociation in H₂, HD, and D₂, obtained by an electron-ion coincidence method, *J. Phys. B At. Mol. Phys.*, *9*, 315–331.
- Bartlett, P. J., and A. T. Stelbovics (2004), Electron-impact ionization cross sections for elements Z = 1 to Z = 54, *At. Data Nucl. Data Tables*, *86*, 235–265, doi:10.1016/j.adt.2003.11.006.
- Brackmann, R. T., W. L. Fite, and R. H. Neynaber (1958), Collisions of electrons with hydrogen atoms. III. Elastic scattering, *Phys. Rev.*, *112*, 1157–1161, doi:10.1103/PhysRev.112.1157.

- Bray, I., D. A. Konovalov, and I. E. McCarthy (1991), Electron scattering by atomic hydrogen: Elastic and inelastic phenomena at 13.9–200 eV, *Phys. Rev. A*, *44*, 5586–5598, doi:10.1103/PhysRevA.44.5586.
- Brunger, M. J., and S. J. Buckman (2002), Electron-molecule scattering cross-sections. I. Experimental techniques and data for diatomic molecules, *Phys. Rep.*, *357*, 215–458.
- Burke, P. G., and K. Smith (1962), The low-energy scattering of electrons and positrons by hydrogen atoms, *Rev. Mod. Phys.*, *34*, 458–502, doi:10.1103/RevModPhys.34.458.
- Capone, L. A., R. C. Whitten, S. S. Prasad, and J. Dubach (1977), The ionospheres of Saturn, Uranus, and Neptune, *Astrophys. J.*, *215*, 977–983.
- Chung, Y. M., E.-M. Lee, T. Masuoka, and J. A. R. Samson (1993), Dissociative photoionization of H₂ from 18 to 124 eV, *J. Chem. Phys.*, *99*, 885–889.
- Coates, A. J., A. D. Johnstone, J. J. Sojka, and G. L. Wrenn (1985), Ionospheric photoelectrons observed in the magnetosphere at distances up to 7 Earth radii, *Planet. Space Sci.*, *33*, 1267–1275, doi:10.1016/0032-0633(85)90005-4.
- Connerney, J. E. P., and J. H. Waite Jr. (1984), New model of Saturn's ionosphere with an influx of water from the rings, *Nature*, *312*, 136–138.
- Cravens, T. E., J. Vann, J. Clark, J. Yu, C. N. Keller, and C. Brull (2004), The ionosphere of Titan: An updated theoretical model, *Adv. Space Res.*, *33*, 212–215, doi:10.1016/j.asr.2003.02.012.
- Davies, D. K., L. E. Kline, and W. E. Bies (1989), Measurements of swarm parameters and derived electron collision cross sections in methane, *J. Appl. Phys.*, *65*, 3311–3323.
- Davis, L. Jr., and E. J. Smith (1990), A model of Saturn's magnetic field based on all available data, *J. Geophys. Res.*, *95*, 15,257–15,261, doi:10.1029/JA095iA09p15257.
- Dujardin, G., M. J. Besnard, L. Hellner, and Y. Malinovitch (1987), Double photoionization of H₂: An experimental test of electronic-correlation models in molecules, *Phys. Rev. A*, *35*, 5012–5019.
- Fox, J. L. (2007), Near-terminator Venus ionosphere: How Chapman-esque?, *J. Geophys. Res.*, *112*, E04S02, doi:10.1029/2006JE002736.
- Fox, J. L., and K. E. Yeager (2006), Morphology of the near-terminator Martian ionosphere: A comparison of models and data, *J. Geophys. Res.*, *111*, A10309, doi:10.1029/2006JA011697.
- Galand, M., J. Liliensten, D. Toubanc, and S. Maurice (1999), The ionosphere of Titan: Ideal diurnal and nocturnal cases, *Icarus*, *140*, 92–105, doi:10.1006/icar.1999.6113.
- Galand, M., R. V. Yelle, A. J. Coates, H. Backes, and J.-E. Wahlund (2006), Electron temperature of Titan's sunlit ionosphere, *Geophys. Res. Lett.*, *33*, L21101, doi:10.1029/2006GL027488.
- Gérard, J.-C., and V. Singh (1982), A model of energy deposition of energetic electrons and EUV emission in the Jovian and Saturnian atmospheres and implications, *J. Geophys. Res.*, *87*, 4525–4532.
- Hiraki, Y., and C. Tao (2008), Parameterization of ionization rate by auroral electron precipitation in Jupiter, *Ann. Geophys.*, *26*, 77–86.
- Hubbard, W. B., et al. (1997), Structure of Saturn's Mesosphere from the 28 SGR occultations, *Icarus*, *130*, 404–425.
- Huestis, D. L. (2008), Hydrogen collisions in planetary atmospheres, ionospheres, and magnetospheres, *Planet. Space Sci.*, *56*, 1733–1743, doi:10.1016/j.pss.2008.07.012.
- Jain, A., and K. L. Baluja (1992), Total (elastic plus inelastic) cross sections from diatomic and polyatomic molecules at 10–5000 eV: H₂, Li₂, HF, CH₄, N₂, CO, C₂H₂, HCN, O₂, HCl, H₂S, PH₃, SiH₄, and CO₂, *Phys. Rev. A*, *45*, 202–218, doi:10.1103/PhysRevA.45.202.
- Jurac, S., and J. D. Richardson (2005), A self-consistent model of plasma and neutrals at Saturn: Neutral cloud morphology, *J. Geophys. Res.*, *110*, A09220, doi:10.1029/2004JA010635.
- Kim, Y. H., and J. L. Fox (1991), The Jovian ionospheric E region, *Geophys. Res. Lett.*, *18*, 123–126.
- Kim, Y. H., and J. L. Fox (1994), The chemistry of hydrocarbon ions in the Jovian ionosphere, *Icarus*, *112*, 310–325, doi:10.1029/90GL02587.
- Kliore, A. J., G. F. Lindal, I. R. Patel, D. N. Sweetnam, and H. B. Hotz (1980a), Vertical structure of the ionosphere and upper neutral atmosphere of Saturn from the Pioneer radio occultation, *Science*, *207*, 446–449.
- Kliore, A. J., I. R. Patel, G. F. Lindal, D. M. Sweetnam, H. B. Hotz, J. H. Waite Jr., and T. R. McDonough (1980b), Structure of the ionosphere and atmosphere of Saturn from Pioneer 11 radio occultation, *J. Geophys. Res.*, *85*, 5857–5870.
- Kliore, A. J., A. F. Nagy, E. A. Marouf, A. Anabtawi, E. Barbini, D. U. Fleischman, and D. S. Kahan (2009), Midlatitude and high-latitude electron density profiles in the ionosphere of Saturn obtained by Cassini radio occultation observations, *J. Geophys. Res.*, *114*, A04315, doi:10.1029/2008JA013900.

- Kossmann, H., O. Schwarzkopf, B. Kämmerling, W. Braun, and V. Schmidt (1989a), Photoionization cross section of H₂, *J. Phys. B At. Mol. Opt. Phys.*, **22**, L411–L414.
- Kossmann, H., O. Schwarzkopf, B. Kämmerling, W. Braun, and V. Schmidt (1989b), Unexpected behavior of double photoionization in H₂, *Phys. Rev. Lett.*, **63**, 2040–2043.
- LaBahn, R. W., and J. Callaway (1970), Differential cross sections for the elastic scattering of 1- to 95-eV electrons from helium, *Phys. Rev. A*, **2**, 366–369, doi:10.1103/PhysRevA.2.366.
- Lindal, G. F., D. N. Sweetnam, and V. R. Eshleman (1985), The atmosphere of Saturn: An analysis of the Voyager radio occultation measurements, *Astron. J.*, **90**, 1136–1146.
- Liu, X., and D. E. Shemansky (2006), Analysis of electron impact ionization properties of methane, *J. Geophys. Res.*, **111**, A04303, doi:10.1029/2005JA011454.
- Liu, X., D. E. Shemansky, S. M. Ahmed, G. K. James, and J. M. Ajello (1998), Electron-impact excitation and emission cross sections of the H₂ Lyman and Werner systems, *J. Geophys. Res.*, **103**, 26,739–26,758.
- Lummerzheim, D., and J. Liliensten (1994), Electron transport and energy degradation in the ionosphere: evaluation of the numerical solution. Comparison with laboratory experiments and auroral observations, *Ann. Geophys.*, **12**, 1039–1051.
- Lummerzheim, D., M. H. Rees, and H. R. Anderson (1989), Angular dependent transport of auroral electrons in the upper atmosphere, *Planet. Space Sci.*, **37**, 109–129.
- Majeed, T., and J. C. McConnell (1991), The upper ionospheres of Jupiter and Saturn, *Planet. Space Sci.*, **39**, 1715–1732.
- Matcheva, K. I., D. F. Strobel, and F. M. Flasar (2001), Interaction of gravity waves with ionospheric plasma: Implications for Jupiter's ionosphere, *Icarus*, **152**, 347–365, doi:10.1006/icar.2001.6631.
- Mayol, R., and F. Salvat (1997), Total and transport cross sections for the elastic scattering of electrons by atoms, *At. Data Nucl. Data Tables*, **65**, 55–154.
- McElroy, M. B. (1973), The ionospheres of the major planets, *Space Sci. Rev.*, **14**, 460–473.
- Mendillo, M., L. Moore, J. Clarke, I. Mueller-Wodarg, W. S. Kurth, and M. L. Kaiser (2005), Effects of ring shadowing on the detection of electrostatic discharges at Saturn, *Geophys. Res. Lett.*, **32**, L05107, doi:10.1029/2004GL021934.
- Moore, L. E., and M. Mendillo (2007), Are plasma depletions in Saturn's ionosphere a signature of time-dependent water input?, *Geophys. Res. Lett.*, **34**, L12202, doi:10.1029/2007GL029381.
- Moore, L. E., M. Mendillo, I. C. F. Mueller-Wodarg, and D. L. Murr (2004), Modeling of global variations and ring shadowing in Saturn's ionosphere, *Icarus*, **172**, 503–520, doi:10.1016/j.icarus.2004.07.007.
- Moore, L., A. F. Nagy, A. J. Kliore, I. Mueller-Wodarg, J. D. Richardson, and M. Mendillo (2006), Cassini radio occultations of Saturn's ionosphere: Model comparisons using a constant water flux, *Geophys. Res. Lett.*, **33**, L22202, doi:10.1029/2006GL027375.
- Moore, L., M. Galand, I. Mueller-Wodarg, R. Yelle, and M. Mendillo (2008), Plasma temperatures in Saturn's ionosphere, *J. Geophys. Res.*, **113**, A10306, doi:10.1029/2008JA013373.
- Moore, L., M. Galand, I. Mueller-Wodarg, and M. Mendillo (2009), Response of Saturn's ionosphere to solar radiation: Testing parameterizations for thermal electron heating and secondary ionization processes, *Planet. Space Sci.*, doi:10.1016/j.pss.2009.05.001, in press.
- Moses, J. I., and S. F. Bass (2000), The effects of external material on the chemistry and structure of Saturn's ionosphere, *J. Geophys. Res.*, **105**, 7013–7052, doi:10.1029/1999JE001172.
- Moses, J. I., B. Bezard, E. Lellouch, G. R. Gladstone, H. Feuchtgruber, and M. Allen (2000a), Photochemistry of Saturn's atmosphere, I. Hydrocarbon chemistry and comparisons with ISO observations, *Icarus*, **143**, 244–298, doi:10.1006/icar.1999.6270.
- Moses, J. I., E. Lellouch, B. Bezard, G. R. Gladstone, H. Feuchtgruber, and M. Allen (2000b), Photochemistry of Saturn's atmosphere, II. Effects of an influx of external oxygen, *Icarus*, **145**, 166–202, doi:10.1006/icar.1999.6320.
- Mueller-Wodarg, I. C. F., M. Mendillo, R. V. Yelle, and A. D. Aylward (2006), A global circulation model of Saturn's thermosphere, *Icarus*, **180**, 147–160, doi:10.1016/j.icarus.2005.09.002.
- Nagy, A. F., et al. (2006), First results from the ionospheric radio occultations of Saturn by the Cassini spacecraft, *J. Geophys. Res.*, **111**, A06310, doi:10.1029/2005JA011519.
- Neupert, W. M. (2006), Variability of the solar soft X-ray irradiance (0.6–2.5 nm) with solar activity, *Adv. Space Res.*, **37**, 238–245, doi:10.1016/j.asr.2005.01.072.
- Porco, C. C., et al. (2006), Cassini observes the active South Pole of Enceladus, *Science*, **311**, 1393–1401.
- Rees, M. H. (1989), *Physics and Chemistry of the Upper Atmosphere*, Cambridge Atmos. Space Sci. Ser., Cambridge Univ. Press, Cambridge, U. K.
- Régo, D., R. Prangé, and J.-C. Gérard (1994), Auroral Lyman alpha and H₂ bands from the giant planets: 1. Excitation by proton precipitation in the Jovian atmosphere, *J. Geophys. Res.*, **99**, 17,075–17,094, doi:10.1029/93JE03432.
- Richards, P. G., and D. G. Torr (1985), The altitude variation of the ionospheric photoelectron flux: A comparison of theory and measurement, *J. Geophys. Res.*, **90**, 2877–2884, doi:10.1029/JA090iA03p02877.
- Richards, P. G., and D. G. Torr (1988), Ratios of photoelectron to EUV ionization rates for aeronomic studies, *J. Geophys. Res.*, **93**, 4060–4066, doi:10.1029/JA093iA05p04060.
- Richards, P. G., J. A. Fennelly, and D. G. Torr (1994), EUVAC: A solar EUV flux model for aeronomic calculations, *J. Geophys. Res.*, **99**, 8981–8992. (Correction, *J. Geophys. Res.*, **99**, 13,283–13,284, 1994.)
- Richards, P. G., T. T. N. Woods, and W. K. Peterson (2006), HEUVAC: A new high resolution solar EUV proxy model, *Adv. Space Res.*, **37**, 315–322, doi:10.1016/j.asr.2005.06.031.
- Samson, J. A. R., G. N. Haddad, T. Masuoka, P. N. Pareek, and D. A. L. Kilcoyne (1989), Ionization yields, total absorption, and dissociative photoionization cross sections of CH₄ from 110–950 Å, *J. Chem. Phys.*, **90**, 6925–6932.
- Schlesier, A. C., and M. J. Buonsanto (1999), The Millstone Hill ionospheric model and its application to the May 26–27, 1990, ionospheric storm, *J. Geophys. Res.*, **104**, 22,453–22,468, doi:10.1029/1999JA000250.
- Schunk, R. W., and A. F. Nagy (2000), *Ionospheres: Physics, Plasma Physics, and Chemistry*, Atmos. Space Sci. Ser., Cambridge Univ. Press, Cambridge, U. K.
- Smith, G. R., D. E. Shemansky, J. B. Holberg, A. L. Broadfoot, B. R. Sandel, and J. C. McConnell (1983), Saturn's upper atmosphere from the Voyager 2 EUV solar and stellar occultations, *J. Geophys. Res.*, **88**, 8667–8678, doi:10.1029/JA088iA11p08667.
- Solomon, S. C., S. M. Bailey, and T. N. Woods (2001), Effect of solar soft X-rays on the lower ionosphere, *Geophys. Res. Lett.*, **28**, 2149–2152, doi:10.1029/2001GL012866.
- Stone, P. M., Y.-K. Kim, and J. P. Desclaux (2002), Electron-impact cross sections for dipole- and spin-allowed excitations of hydrogen, helium, and lithium, *J. Res. Natl. Inst. Stand. Technol.*, **107**, 327–337.
- Straub, H. C., P. Renault, B. G. Lindsay, K. A. Smith, and R. F. Stebbings (1996), Absolute partial cross sections for electron-impact ionization of H₂, N₂, and O₂ from threshold to 1000 eV, *Phys. Rev. A*, **54**, 2146–2153, doi:10.1103/PhysRevA.54.2146.
- Tobiska, W. K. (2004), SOLAR2000 irradiances for climate change research, aeronomy and space system engineering, *Adv. Space Res.*, **34**, 1736–1746, doi:10.1016/j.asr.2003.06.032.
- Tobiska, W. K., and S. D. Bouwer (2006), New developments in SOLAR2000 for space research and operations, *Adv. Space Res.*, **37**, 347–358, doi:10.1016/j.asr.2005.08.015.
- Torr, M. R., D. G. Torr, R. A. Ong, and H. E. Hinteregger (1979), Ionization frequencies for major thermospheric constituents as a function of solar cycle 21, *Geophys. Res. Lett.*, **6**, 771–774.
- Tyler, G. L., V. R. Eshleman, J. D. Anderson, G. S. Levy, G. F. Lindal, G. E. Wood, and T. A. Croft (1981), Radio science investigation of the Saturn system with Voyager 1: Preliminary results, *Science*, **212**, 201–206.
- Tyler, G. L., V. R. Eshleman, J. D. Anderson, G. S. Levy, G. F. Lindal, G. E. Wood, and T. A. Croft (1982), Radio science with Voyager 2 at Saturn: Atmosphere and ionosphere and the masses of Mimas, Tethys, and Iapetus, *Science*, **215**, 553–558.
- van Wingerden, B., R. W. Wagenaar, and F. J. de Heer (1980), Total cross sections for electron scattering by molecular hydrogen, *J. Phys. B At. Mol. Opt. Phys.*, **13**, 3481–3491.
- Verner, D. A., G. J. Ferland, K. T. Korista, and D. G. Yakovlev (1996), Atomic data for astrophysics. II. New analytic fits for photoionization cross sections of atoms and ions, *Astrophys. J.*, **465**, 487–498, doi:10.1086/177435.
- Waite, J. H., Jr. (1981), The ionosphere of Saturn, thesis, Univ. of Mich., Ann Arbor.
- Woods, T. N. (2008), Recent advances in observations and modeling of the solar ultraviolet and X-ray spectral irradiance, *Adv. Space Res.*, **42**, 895–902, doi:10.1016/j.asr.2007.09.026.
- Woods, T. N., et al. (2000), TIMED Solar EUV Experiment, *Phys. Chem. Earth, Part C*, **25**, 393–396.
- Woods, T. N., F. G. Eparvier, S. M. Bailey, P. C. Chamberlin, J. Lean, G. J. Rottman, S. C. Solomon, W. K. Tobiska, and D. L. Woodraska (2005), Solar EUV Experiment (SEE): Mission overview and first results, *J. Geophys. Res.*, **110**, A01312, doi:10.1029/2004JA010765.

Yan, M., H. R. Sadeghpour, and A. Dalgarno (1998), Photoionization cross sections of He and H₂, *Astrophys. J.*, 496, 1044–1050, doi:10.1086/305420. (Erratum, *Astrophys. J.*, 559, 1194, doi:10.1086/322775, 2001.)

B. Charnay, Ecole Normale Supérieure de Lyon, 46 Allée d'Italie, F-69007 Lyon, France.

M. Galand and I. Mueller-Wodarg, Space and Atmospheric Physics Group, Department of Physics, Imperial College London, Prince Consort Road, London SW7 2AZ, UK. (m.galand@imperial.ac.uk)

M. Mendillo and L. Moore, Center for Space Physics, Boston University, 725 Commonwealth Avenue, Boston, MA 02215, USA.